Imaging an Active Normal Fault in Alluvium by High-Resolution Magnetic and Electromagnetic Surveys

by

Peter C. La Femina, Charles B. Connor, John A. Stamatakos, David A. Farrell

all at Center for Nuclear Waste Regulatory Analyses, Southwest Research Institute, 6220 Culebra Rd., San Antonio, TX, 78238-5166, USA, plafemina@swri.edu

to be submitted to Environmental & Engineering Geosciences

draft of 08/01/00

Key Terms: Magnetics, Paleomagnetics, Electromagnetics, Soil Conductivity, Fault Zones, Allostratigraphy

Abstract

High-resolution geophysical investigations can dramatically improve paleoseismic studies and the characterization of fault zones. Here, a detailed magnetic survey indicates that 60-70 m of vertical separation has occurred on the South Crater Flat fault (SCFF), Nevada, since the eruption of basaltic lavas approximately 3.75 Ma. These values give an average throw rate of 0.017 mm/yr and an average slip rate of 0.02 mm/yr, roughly one order of magnitude greater than

Quaternary slip rates derived from trench studies of alluvial stratigraphy across the fault. The Pliocene basalt has a reversed remanent magnetization (inclination = -61.7°, declination = 162.0°, intensity of magnetization ≈10 A/m), creating a > 1000 nT anomaly across the SCFF. Forward models of three magnetic profiles reveal several synthetic and antithetic normal faults west of the SCFF and a decrease in displacement on the SCFF from north to the south. Electromagnetic surveys reveal a 140-200 m wide, 1.5-2.5 mS/m electrical conductivity anomaly parallel to the fault zone in the alluvial wedge of the hanging wall. This anomaly correlates with active drainageways and reflects lateral variations in allostratigraphy, produced by Quaternary slip on the SCFF, that complicate trench stratigraphy. Variations in clay content and porosity most likely cause the electrical anomaly. These results indicate that displacement has been distributed across several faults and that the long-term average slip rate is higher than Quaternary slip rates derived from trench studies alone. Thus, these geophysical methods provide an areal and temporal perspective on the fault zone not possible with traditional fault characterization techniques.

Introduction

Gaining insight into the geometry and physical properties of fault zones is important in two ways. First, normal faults and their damage zones (Sibson, 1977; Caine et al., 1996, Seront et al., 1998) can complicate paleoseisimic investigations because deformation within these such fault zones can be diffuse and geologically complex. This complexity needs to be accounted for in estimates of the rates and models for the mechanisms of seismic activity. Second, normal fault zones often have a profound affect on meteoric infiltration and groundwater flow in the

unsaturated zone because these structures can increase infiltration and transmissivity through secondary permeability. Flow in such zones limits opportunities for dilution or sorption of some contaminants, including radionuclides, compared to porous flow in an isotropic and uniform alluvial media (Bagtzoglou et al., 1997; Ferrill et al., 1999).

Here, we apply high-resolution magnetic, paleomagnetic, and electromagnetic (EM) methods to delineate and map displacement across the South Crater Flat fault (SCFF), an active normal fault in the southern Crater Flat basin, southwest Nevada (Faulds et al., 1994; Taylor, 1996) (Figure 1). This area is of particular interest because of the SCFF's proximity to the proposed geological repository for high-level radioactive waste at Yucca Mountain (YM), Nevada (U.S. National Research Council, 1995). Faults in the YM region are being evaluated for potential earthquake hazards (Civilian Radioactive Waste Management System Management & Operating Contractor, 1998) and hydrologic properties that may affect migration and retardation of radionuclides (Ferrill et al., 1999). Therefore, evaluation of the uncertainties about earthquake hazards and hydrologic conditions at the site is a critical component of both the YM site assessment by the Department of Energy and independent evaluation by the Nuclear Regulatory Commission of the adequacy of that assessment. Although many normal faults are mapped in Crater Flat and YM, we selected the SCFF for detailed study because the fault has been trenched in two locations (Taylor, 1996), and the fault juxtaposes 3.73 +/- 0.02 Ma basalt (Fleck et al., 1996) against Quaternary (< 300 ka) alluvium (Faulds et al., 1994; Peterson et al., 1995), providing constraints on the timing of fault zone development and sharp magnetic contrast.

The South Crater Flat Fault

The Crater Flat fault system is located west-southwest of the proposed YM repository within the Crater Flat basin (Figure 1). This basin is actively subsiding, with sediment accumulation rates up to 0.03 mm/yr (Stamatakos et al., 1997), and is bound on the west by the east-dipping Bare Mountain fault. The Crater Flat fault and nearby faults are predominantly west-dipping and sole into the east-dipping Bare Mountain fault at depth (Fridrich et al., 1999; Stamatakos et al., 2000). The Crater Flat fault itself consists of two segments. The segments have a cumulative length of 18 km, and an average dip of 70° down to the west (Simonds et al., 1995; Simonds et al., 1996).

The SCFF, the southern segment of the Crater Flat fault, is delineated by faulted basalt - alluvium contacts, fractured carbonate-cemented alluvium, and linear drainageways (Faulds et al., 1994; Simonds et al., 1996). The fault has little surface expression in the northern part of this segment and alluvium is exposed at the surface on both sides of the fault (Figure 2). However, basalt crops out in drainageways in the footwall, indicating the alluvial veneer is thin, only 1-3 m thick. A topographic step across the fault is more prominent in the southern part of the segment and basaltic lavas crop out over a broad area of the footwall. This geometry creates a narrow strip of alluvium in the hanging wall between the lavas in the footwall and a vent and dike complex to the west. This vent and dike complex is presumed to be the source of the lava flows (Figure 1).

Two allostratigraphic units have been mapped in this part of the Crater Flat basin (Figure 2). These units are the Late Black Cone alluvium and the Crater Flat alluvium (Faulds et al., 1994; Peterson et al., 1995). The Late Black Cone alluvium is Pleistocene age (≈17 - 39 ka), occurs in the footwall and hanging wall of the SCFF, and is identified in the field by its well-

developed pavement and soil horizons, and in air photos by its darker color. The Crater Flat alluvium is Late Holocene age (≈1.3 ka), occurs in active drainageways or washs in the hanging wall of the SCFF, and is identified in the field by its lack of developed pavement and soil horizons.

The sequence of Pliocene basalt and alluvium exposed across the SCFF overlies Miocene-Pliocene age (12.7-3.75 Ma) alluvium and the Tiva Canyon member of the Paintbrush Tuff, a Miocene (12.7 Ma) ignimbrite that crops out at YM (Frizzell and Shulters, 1990; Day et al., 1997). This stratigraphy is observed in nearby wells (Carr, 1982), where approximately 100 m of alluvium exists between the Tiva Canyon tuff and Pliocene basalt.

Slip on the fault is dominantly dip-slip with a minor component of left oblique-slip (Taylor, 1996). Cumulative displacements across the fault are unknown, but paleoseismic studies in two trenches across the SCFF (Figure 2) suggest Quaternary (<250 ka) displacements between 2.0 and 3.0 m (Taylor, 1996). The southernmost trench (CFF-1a, Figure 2) intersects the SCFF. Here, basaltic lavas in the footwall are clearly offset from alluvium in the hanging wall. The northernmost trench (CFF-1, Figure 2) reveals fracturing of the alluvium in the hanging wall but does not intersect basalt in the footwall or hanging wall. Nevertheless, small offsets are observed across fractures in CFF-1, consistent with the sense of displacement of the SCFF. Dips of 82° and 90° were measured on fracture surfaces in both trenches (Taylor, 1996). Precipitation of caliche in some of the fractures suggests that these fractures acted as preferred pathways for infiltration of meteoric water.

Taylor (1996) identified at least three <250 ka surface faulting events in the two trenches, with cumulative vertical offset of 24-65 cm, for a maximum vertical slip rate of 0.002 mm/yr.

Taylor (1996) noted that tectono-stratigraphic units were difficult to correlate between the trenches and suggested that the lack of correlation might arise from a complex history of sedimentation in the fault zone, along-strike variations in slip history, and perhaps a component of strike-slip (Taylor, 1996). These difficulties, present in many paleoseismology investigations (e.g., McCalpin, 1996), illustrate the need to develop new and better techniques to image the shallow subsurface across fault zones like the SCFF. Utilizing geophysical techniques, we produced maps of magnetic field and electrical conductivity within a 0.53 km^2 area about the N10-20°E trending fault (Figures 3 and 4). In addition, a topographic map of the area was produced and the positions of the two paleoseismic trenches were outlined utilizing differential GPS (DGPS) surveying techniques. Augmented with paleomagnetic analyses, the maps were used to model the SCFF with the goal of more fully delineating the structure of the SCFF for independant paleoseismic and hydrologic assessments.

Paleomagnetism

Samples for paleomagnetic analyses were collected from 8 sites in Crater Flat (Figure 1). Characteristic and secondary magnetizations were isolated using progressive alternating field (af) and thermal demagnetization (Figures 5a and 5b). Magnetic components isolated during demagnetization experiments were determined from visual inspection of the linear segments on vector end-point diagrams. Component directions were determined from a least squares fit of the observed linear trajectories (e.g., Kirschvink, 1980). Sample directions were combined to form site means using simple vector addition giving unit weight to each sample direction. Statistical parameters were calculated following Fisher (1953).

Intensities of the natural remanent magnetizations (NRM) range between about 2.4 and 25 A/m, and average 10.01 A/m (Table 1). Both af and thermal demagnetization successfully isolated a characteristic remanent magnetization (ChRM) in the samples. Vector end-point diagrams show removal of a weak overprinting direction followed by univectoral decay to the origin (Figures 5a and 5b).

For all samples but those from site PCF5 and PCF8, ChRM directions are south-southeast and moderately to steeply up (Figures 5b and 5c; Table 1). The mean of the direction for the 6 sites with south-southeast and up directions (Dec = 162°, Inc = -62°, α_{95} = 7.4°) is near, but slightly steeper than the expected Pliocene direction for Crater Flat (Dec = 180°, Inc = -57°; assuming present day axial geocentric dipole). This difference may reflect a small component of post-eruption tilting of the basalt flows, or more likely, unaveraged secular variation of the Pliocene geomagnetic field. These paleomagnetic results are similar to those of Champion (1995), who reported uniformly reversed-polarity directions for six Pliocene basalt sites. The reversed polarity is also consistent with the reported radiometric age of 3.73 ± 0.02 Ma (Fleck et al., 1996), which correlates with reversed chron C2Ar of the geomagnetic polarity time scale (Cande and Kent, 1992).

Site PCF5 was located in the footwall of the SCFF, which is exposed in the southern paleoseismic trench. The mean direction of site PCF5 (Dec = 266°, Inc = -60°, α_{95} = 12.5°) appears to be rotated about a vertical axis 104° counterclockwise from the other 6 sites. We suggest that this site may be located within a detached block of basalt within the footwall damage zone of the SCFF. This suggestion is consistent with an approximately 1.5 m wide graben mapped in the north wall of the southern trench (Taylor, 1996). Also note the occurrence

of both normal and reversed polarity magnetizations for these lavas. Forward modeling, however, suggests that the normal polarity lavas do not have significant volume in the map area, although anomalies near the Windy Wash fault, several kilometers east of the SCFF, do suggest the possibility of more extensive normal-polarity flows there (Magsino et al., 1997).

Magnetic Survey

High remanent magnetization of Pliocene basalt and Miocene tuff in the Crater Flat basin create excellent magnetic contrast for mapping subsurface structure (e.g., Kane and Bracken, 1983; Langenhiem, 1995; Connor et al., 1997; Stamatakos et al., 1997). We constructed a magnetic field intensity map of this area using a cesium-vapor magnetometer (Geometrics® model G-858) interfaced to a real-time kinematic, DGPS (Novatel®) with resolution of ±2 cm horizontal and ±10 cm vertical (2 sigma error) (Connor et al., 1997). Approximately 4,000 data points were collected on 17 E-trending traverses across the SCFF and three N-trending tie lines. Spatial resolution of each data point is ± 1 m horizontal (accounting for offsets between the DGPS antenna and the magnetometer). Magnetic data were drift corrected using geomagnetic data gathered at 15 second intervals at a base station magnetometer operating at the site.

Vertical offset (throw) of the Pliocene basalt caused by the SCFF is well-delineated on the magnetic map (Figure 3). In the footwall, the basalt produces a highly complex pattern, with numerous large amplitude, short-wavelength magnetic anomalies. Overall, the magnetic anomaly is negative and is bounded on the west by a narrow positive anomaly with quite consistent amplitude and wavelength. The peak-to-peak amplitude of this anomaly exceeds 1000 nT. The

anomaly is consistent with the vertical offset of lavas that have a strong, reversed-polarity remanent magnetization. Magnetic anomalies persist west of the fault but have lower amplitudes and longer wavelengths, consistent with burial of faulted lava flows beneath alluvium.

Forward modeling of three E-trending magnetic profiles across the SCFF indicates 60-70 m of vertical separation of the basaltic lavas, with a general decrease in throw to the south (Figures 6a-c). Mean directions of magnetization (Table 1) and intensities of remanent magnetization of 10-14 A/m, as measured by the paleomagnetic analyses, were assigned to the Pliocene basalt to prepare these models. Given the strong NRM intensities, it is clear that the magnetization of the basalt is strongly dominated by remanence. Therefore, in the models, susceptibility values are not assigned to the basaltic lavas.

Longer wavelength variation in the magnetic field in the hanging wall was best modeled by including additional normal faults synthetic and antithetic to the SCFF. Normal faults synthetic to the SCFF add 16-36 m of cumulative throw across this fault system. One of the antithetic faults has been inferred north of our study area, based on linear drainageway patterns (Faulds et al.,1994), but the others have not been previously mapped.

The Tiva Canyon tuff is modeled with remanent magnetizations of 5-9 A/m (Rosenbaum et al, 1991), and is assumed to be 85-100 m beneath the Pliocene lavas, consistent with the thickness of the overlying alluvial unit mapped in well USW VH-1 (Carr, 1982). The forward models demonstrate that the Tiva Canyon tuff is offset vertically by 65-75 m, indicating that most of the displacement on the SCFF occurred in the last 3.73 Ma, after eruption of the Pliocene lavas.

Electromagnetic Survey

Noninvasive EM methods are optimal for mapping subtle variations in clay and water content in the unsaturated zone (e.g., Taylor et al., 1992; Sheets and Hendrickx, 1995) and in locating fault zones (McNeill, 1990). We constructed a conductivity map of the survey area using an electromagnetic terrain conductivity meter (Geonics EM-31®) and a DGPS. EM-31 and DGPS measurements were collated during data post-processing using time stamps. Approximately 3,700 EM-31 measurements were made along the same traverses made for magnetic measurements. All conductivity measurements are reported in milliSiemens per meter (mS/m), where a mS/m = 1000/(Ω m).

The EM-31 induces current flow in the half-space (ground) beneath a transmitter coil and measures the primary and secondary magnetic fields at a receiver coil (McNeill, 1980). The primary magnetic field is produced directly by the transmitter and is sent to the receiver by a direct electrical connection. The secondary magnetic field is produced by electrical currents in the conducting host material (e.g., rock or alluvium). Apparent conductivity is directly proportional to the amplitude of the secondary magnetic field and the phase shift between the primary and secondary magnetic fields, measured by the EM-31 at a fixed coil separation (McNeill, 1980). The depth and volume of rock over which earth conductivities are integrated to produce a single apparent conductivity measurement depend on the distance of coil separation and the orientation of the coils (e.g., Parasnis, 1986). The EM-31 has a fixed coil separation of 3.7 m and was operated with the coils in a vertical dipole orientation. Because the SCFF survey was in an area of low conductivities, maximum depth of penetration is up to 7 m (McNeill, 1980).

The conductivity map (Figure 4) delineates the SCFF as a sharp change from comparatively high conductivities measured on the basalt east of the fault zone (5-10 mS/m) to the lower conductivity alluvium west of the fault zone (1-5 mS/m). This step across the fault is accentuated by a 140-200 m wide band of low conductivity values (1.5-2.5 mS/m) that trends parallel to the fault (Figure 4). This narrow band of lower conductivities correlates with active drainageways in the Crater Flat alluvium and the location of vertical fractures in the alluvium adjacent to the SCFF, as evidenced by trenching studies (Taylor, 1996).

Traverses were made across the SCFF with a second electromagnetic conductivity meter (Geonics® EM-34) to achieve slightly deeper penetration of conductivity measurements (McNeill, 1980). The EM-34 traverses were made using vertical and horizontal dipoles and a 20-m coil separation. Vertical dipoles integrate conductivity to depths of about 30 m and are most sensitive to conductivity variation at depths of 10-20 m. Horizontal dipoles integrate conductivity to a depth of about 15 m and are most sensitive to near surface conductivity. For the comparatively shallow, horizontal dipole measurements, the results are consistent with the EM-31 survey (Figure 7). Low conductivities were identified in the hanging wall and there is an abrupt increase in conductivity in the footwall associated with the shallow Pliocene basalt. The vertical dipole measurements show generally higher conductivity, especially in the hanging wall (Figure 7). As in the horizontal dipole measurements, conductivity decreases from west to east up to the fault zone. Within the fault zone, conductivity rapidly varies between 1 and 6 mS/m.

Discussion

The paleomagnetic measurements greatly reduce uncertainty in the magnetic models because

they place bounds on the remanent magnetization. Although the forward models are indeterminate, vertical offset of the basaltic lavas across the SCFF cannot vary substantially from 60-70 m without a large departure from the measured remanent magnetizations. The long-term vertical slip rate across the SCFF, given 60-70 m of throw and an age of 3.75 Ma for the basalt, is 0.016-0.019 mm/yr. Fault dip is not well-constrained by the magnetic models. Nevertheless, assuming dips between 55° and 65° (Simonds et al., 1995), a dip-slip of 65-85 m and a slip rate of 0.017–0.023 mm/yr are derived, compared to a 0.002 mm/yr rate (Taylor, 1996) based on the paleoseismic results. This order of magnitude discrepancy suggests that either the slip rate is substantially lower in the Quaternary than during the Pliocene, or that the trenching studies do not fully capture the record of slip deduced from the forward models of the magnetic data, because of the shallowness of the trenches and the complex, distributed nature of the fault in the near surface.

An interpretation of the electrical conductivity variation across the SCFF emerges by comparing maps of magnetic field, conductivity (EM-31), and geology, and traverses of conductivity (EM-34). The highest electrical conductivity values occur in the footwall and are related to the basalt. North of the exposed basalt, higher conductivities in the Late Black Cone alluvium, as well as outcropping basalt in drainageways, (Faulds et al., 1994; Peterson et al., 1995) indicate that this allostratigraphic unit forms a thin veneer on top of the Pliocene lava flows in the footwall. The forward models of the magnetic data indicate that the Pliocene basalt is too deep in the hanging wall to directly influence the measured conductivity in either the EM-31 or EM-34 surveys. Thus, the remarkably consistent low conductivity zone parallel to the fault (Figure 4) cannot be directly attributed to variation in depth to the basalt within the hanging wall.

Instead, the electrical anomaly in the hanging wall of the SCFF correlates with active drainageways and reflects lateral variations in allostratigraphy. These variations are caused by incision of the Late Black Cone alluvium by the Crater Flat alluvium in active drainageways. Active drainageways exist parallel and adjacent to the SCFF for two reasons. First, vertical offset on the SCFF has created a topographic gradient toward the fault and a more resistant backstop for surface water drainage. Paleochannels mapped in paleoseismic trench CFF-1a (Figure 2) demonstrate that this phenomena has occurred along the SCFF throughout the Quaternary (Taylor, 1996). Surprisingly, the lowest electrical conductivity values occur between the SCFF and the nearest antithetic fault modeled from the magnetic data. This is especially clear in magnetic profiles a and b (Figures 6a-6b). This correlation suggests that even these minor, buried antithetic faults influence the near-surface hydrogeology. Second, slip on the SCFF has created a fault zone up to 2 m wide, evidenced by caliche filled fractures and rotated blocks of basalt in the fault zone, as suggested by the paleomagnetic data and trench studies (Taylor, 1996). This fault zone may enhance meteoric infiltration and localize drainageway formation. The lateral variations in allostratigraphy west of the SCFF are significant, because two units of varying clay content and porosity, the Late Black Cone and Crater Flat alluvium, are juxtaposed. These parameters control the bulk soil electrical conductivity by affecting the pore moisture content and salinity, and field capacity.

More quantitative treatment of the electrical conductivity data is uncertain because of the indeterminate source of the electrical anomaly. Nevertheless, the effect of pore moisture content and salinity on soil conductivity can be evaluated using Archie's law (Archie, 1942), here expressed as:

$$\zeta = \frac{1000}{a\varphi^{-m}s^{-n}\rho} \qquad (1)$$

where ζ is soil conductivity (mS/m), φ is the alluvium porosity, s is the fraction of pore space containing water, ρ is the resistivity of the pore water (Ωm), and $a = 1.5$, $m = 2$, and $n = 2$ are empirically derived constants (Telford et al., 1976). Assuming $\varphi = 0.4$ for the alluvium, the observed variation in soil electrical conductivity in the alluvium (Figures 6a-c and 7) is found using $0.1 < s < 0.3$ and $1 < \rho < 3$ (Mualem and Friedman, 1991) (Figure 8). Variations in pore moisture salinity (i.e., the resistivity of the pore water) due to increased infiltration, variations in clay content, or both can account for the observed change in conductivity in the hanging wall of the SCFF. Changes in the pore fraction containing water can also account for the observed soil conductivities. For example, if the field capacity of the Late Black Cone alluvium is greater than that of the Crater Flat alluvium, the former will have a greater soil conductivity after an equivalent amount of precipitation, assuming no variation in pore moisture salinity. The field capacity of a material is controlled by its porosity and permeability. Fracturing of a material will decrease its field capacity by increasing secondary porosity and permeability. Therefore, the low conductivity anomaly adjacent to the fault may be caused by fault zone deformation, where the deformation has increased the field capacity of the Crater Flat alluvium, thereby enhancing infiltration. Without infiltration data, however, this mechanism is speculative and we cannot conclude if the electrical conductivity anomaly is produced by variable clay content, water content, porosity, or some combination of the three.

Conclusions

Joint interpretation of magnetic, paleomagnetic, and electromagnetic data successfully delineated and mapped the offset across the SCFF, providing a greater areal perspective of the fault zone. The long-term slip rates derived from forward models of magnetic data demonstrate order of magnitude higher rates then that determined through trench studies. Continued vertical offset in the Quaternary resulted in the formation of drainageways adjacent to the SCFF and lateral variations in allostratigraphy, well illustrated by mapped electrical conductivity anomalies adjacent to the SCFF.

Acknowledgments: The authors thank Britt Hill, Ron Martin, and Darrell Sims for their assistance in the field. Reviews by Lawrence McKague and Darrell Sims improved the manuscript. Rebecca Emmott provided expert manuscript preparation assistance. This paper was prepared as a result of work performed at the Center for Nuclear Waste Regulatory Analyses (CNWRA) for the U.S. Nuclear Regulatory Commission (NRC) under contract NRC-02-97-009. This paper is an independent product of the CNWRA and does not necessarily reflect the views or regulatory position of NRC.

REFERENCES

Archie, G.E., 1942, The electrical resistivty log as an aid in determining some reservoir characteristics, Trans. Am. Inst. Min. Metall. Pet. Eng., 146: 54-62.

Bagtzoglou, A.C.; Pearcy, E.C.; Stothoff, S.A.; Wittmeyer, G.W. ; and Coleman, N.M., 1997, *Unsaturated and Saturated Flow Under Isothermal Conditions*. NUREG/CR-6513, No. 1. Washington, DC: Nuclear Regulatory Commission: 10-1-10-29.

Caine, J.S.; Evans, J. P.; and Foster, C.B., 1996, Fault zone architecture and permeability structure. Geology 24: 1025-1028.

Cande, S.C., and Kent, D.V., 1992, A new geomagnetic polarity time scale for the late Cretaceous and Cenozoic. Journal of Geophysical Research 97: 13,917-13,951.

Carr, W. J., 1982, Volcano-tectonic history of Crater Flat, southwestern Nevada, as suggested by new evidence from drill hole USW-VH-1 and vicinity, U.S. Geological Survey Open-File Report 82-457, 23 p.

Champion, D.E., 1995, Volcanic episodes near Yucca Mountain as determined by paleomagnetic studies at Lathrop Wells, Crater Flat, and Sleeping Butte: Nevada, U.S. Geological Survey Open File Report 95-562, 10 p.

Civilian Radioactive Waste Management System Management & Operating Contractor, 1998, Probabilistic Seismic Hazard Analyses for Fault Displacement and Vibratory Ground Motion at Yucca Mountain, Nevada, Oakland, California, 180 p.

Connor, C.B.; Lane-Magsino, S.; Stamatakos, J.A.; Martin, R.H.; La Femina, P.C.; Hill, B.E.; and Lieber, S., 1997, Magnetic Surveys help reassess volcanic hazards at Yucca Mountain, Nevada, Eos, Transactions of the American Geophysical Union 78(7): 73,78.

Day, W.C.; Potter, C.J.; Sweetkind, D.S.; Dickson, R.P.; and San Juan, C.A., 1997, Bedrock geologic map of the central block area, Yucca Mountain, Nye County, Nevada, U.S. Geological Survey Miscellaneous Investigations Series Map I-2601.

Faulds, J.E.; Bell, J.W.; Feuerbach, D.L.; and. Ramelli, A.R, 1994, Geologic map of the Crater Flat area, Nevada, *Map 101*, Nev. Bur. of Mines and Geol., Reno.

Ferrill, D.A.; Winterle, J.R.; Wittmeyer, G.; Sims, D.; Colton, S.; Armstrong, A.; and Morris, A.P., 1999, Stressed rock strains groundwater at Yucca Mountain, GSA Today 9, 1-8.

Fisher, R. A., 1953, Dispersion on a sphere, Proceedings of the Royal Society of London, Series A 217: 295–305.

Fleck, R.J.; Turrin, B.D.; Sawyer, D.A.; Warren, R.G.; Champion, D.E.; Hudson, M.R.; Minor,

S.A., 1996, Age and character of basaltic rocks of the Yucca Mountain region, southern Nevada, Journal of Geophysical Research 100: 8,205-8,227.

Fridrich, C.J.; Whitney, J.W.; Hudson, M.R.; and Crowe, B.M., 1999, Late Cenozoic extension, vertical axis rotation, and volcanism in Crater Flat basin, southwest Nevada, in: L.A.Wright and B.W. Troxel, editors, Cenozoic Basins of the Death Valley Region, Geological Society of America Special Paper 333, 169-196.

Frizzell, V.A., and Schulters, J., 1990, Geologic map of the Nevada Test Site, Southern Nevada, U.S. Geological Survey Miscellaneous Investigations Series Map I-2046.

Kane, M.F., and Bracken, R.E., 1983, Aeromagnetic map of Yucca Mountain and surrounding regions, southwest Nevada, U.S. Geological Survey Open-File Report 83-616.

Kirschvink, J. L., 1980, The least-squares line and plane and the analysis of paleomagnetic data, Geophysical Journal of the Royal Astronomical Society 62: 699-718.

Langenheim, V.E., 1995, Magnetic and gravity studies of buried volcanic centers in the Amargosa Desert and Crater Flat, southwest Nevada, U.S. Geological Survey Open-File Report 95-564.

Mackin, P.C.; Lee, M.P.; Jarzemba, M.S.; Baca, R.G.; McCartin, T.J.; and Codell, R.B., 1997,

Activities Related to Development of the U.S. Environmental Protection Agency Yucca Mountain Standard. NUREG/CR-6513, No. 1. Washington, DC: Nuclear Regulatory Commission: 9-1-9-27.

Magsino, S.L.; Connor, C.B.; Hill, B.E.; Stamatakos, J.A.; La Femina, P.C.; Sims, D.A.; and Martin, R.H., 1998, CNWRA ground magnetic surveys in the Yucca Mountain region, Nevada (1996-1997), CNWRA 98-001, Ceneter for Nuclear Waste Regulatory Analyses, San Antonio, TX, 31 p.

McCalpin, J.P., 1996, Paleoseismology in extensional tectonic environments, in J. P. McCalpin, editor, Paleoseismology, Academic Press, San Diego, 85-146.

McNeill, J.D., 1990, Use of electromagnetic methods for groundwater studies, In: S.H. Ward (ed.), Geotechnical and Environmental Geophysics, Investigations in Geophysics No. 5, Society of Exploration Geophysicists, Tulsa, OK, 191-218.

McNeill, J.D., 1980, *Electromagnetic Terrain Conductivity Measurement at Low Induction Numbers.* Technical Note TN-6. Geonics Limited: Mississauga, Ontario: Canada. 15 pp.

Mualem, Y., and Friedman, S. P., 1991, Theoretical prediction of electrical conductivity in saturated and unsaturated soil, Water Resources Research 27: 2,771-2,777.

Parasnis, D.S., 1986, Principles of Applied Geophysics, Fourth Edition, Chapman and Hall: London, 402 pp.

Peterson, F.R.; Bell, J.W.; Dorn, R.I.; Rameli, A.R.; and Ku, T., 1995, Late Quaternary geomorphology and soils in Crater Flat, Yucca Mountain area, southern Nevada, GSA Bulletin, v. 107, no. 4, p. 379-395.

Rosenbaum, J.G.; Hudson, M.R.; and Scott, R.B., 1991, Paleomagnetic constraints on the geometry and timing of deformation at Yucca Mountain, Nevada, Journal of Geophysical Research, 96: 1963-1979.

Seront, B.; Wong, T.F.; Caine, J.S.; Forster, C.B.; and Bruhn, R.H., 1998, Laboratory characterization of hydromechanical properties of a seismogenic fault system, Journal of Structural Geology 20: 865-881.

Sheets, K. R. and Hendrickx, J.M.H., 1995, Noninvasive soil water content measurement using electromagnetic induction, Water Resources Research, 31: 2401-2409.

Sibson, R.H., 1977, Fault rocks and fault mechanisms, Geological Society of London Journal 133: 191-231.

Simonds, W.F.; Whitney, J.W.; Fox, K.F.; Ramelli, A.R.; Yount, J.C. ; Carr, M.D.; Menges,

C.M.; Dickerson, R.P.; and Scott, R.B., 1995, Map Showing Fault Activity in the Yucca Mountain Area, Nye County, Nevada, U.S. Geological Survey Miscellaneous Investigations Series Map 1-2520, scale 1:24,000.

Simonds, W.F.; Fridrich, C.J.; Hoisch, T.D.; and Hamilton, W.B., 1996, A synthesis of detachment fault studies in the Yucca Mountain region, Methods of Seismic Hazard Evaluation, Proceedings of the Topical Meeting on Methods of Seismic Hazards Evaluation, Focus '95, La Grange Park, IL, American Nuclear Society, 107-114.

Stamatakos, J.A.; Connor, C.B.; and Martin, R.H., 1997, Quaternary evolution and basaltic volcanism of Crater Flat, Nevada, from detailed ground magnetic surveys of the Little Cones, Journal of Geology, 105: 319-330.

Stamatakos, J.A.; Hill, B.E.; Ferrill, D.A.; La Femina, P.C.; Sims, D.; Connor, C.B.; Gray, M.B.; Morris, A.P.; and Hall, C.M., 2000, *Composite 13 Million Year Record of Extensional Faulting and Basin Growth of Crater Flat, Nevada.* IM 01402.471.020. San Antonio, Texas: Center for Nuclear Waste Regulatory Analyses.

Taylor, E.M., 1996, Quaternary faulting on the Southern Crater Flat Fault, in J. W. Whitney, editor, Seismotectonic Framework and Characterization of Faulting at Yucca Mountain, Nevada, U.S. Geological Survey Report WBS Number 1.2.3.2.8.3.6, pages 4.10.1-4.10.12.

Taylor, K.; Widmer, M.; and Chesley, M., 1992, Use of transient electromagnetics to define local hydrogeology in an arid alluvial environment, Geophysics 57: 343-352.

Telford, W.M.; Geldart, L. P.; Sheriff, R.E.; and Keys, D.A., 1976, Applied Geophysics, Cambridge University Press, Cambridge, 860 pp.

U.S. National Research Council, 1995, Technical Basis for Yucca Mountain Standards, National Academy Press, Washington, D.C., 206 p.

Zijderveld, J.D.A., 1967, AC demagnetization of rocks: Analysis of results, *in* Collinson, D.W., et al., eds., Methods of Paleomagnetism, Amsterdam, Elsevier Science Publishing: 254–286.

Figure Captions

Figure 1. Map of the study area. The area investigated (designated by paleomagnetic site 5) is located at the northern edge of outcrops of Pliocene basaltic lava flows, and approximately 10 km SW of the proposed high-level radioactive waste repository at Yucca Mountain. Geology from Frizzell and Schulters (1990) and Day et al. (1997), figure modified from Stamatakos et al. (1997). Numbers 1-8 indicate locations of paleomagnetic sites (see Table 1). Dashed line indicates the SCFF.

Figure 2. Air photo of the field area showing the location of the SCFF (solid black line), allostratigraphic units (Crater Flat alluvium(Qfcf), Late Black Cone alluvium (Qflc), and Pliocene basalt (Tb)), paleoseismic trenches (CFF-1, CFF-1a), and active drainageways. Stratigraphy from Faulds et al., (1994).

Figure 3. Magnetic anomaly map across the South Crater Flat fault (same area as Figure 2). Magnetic data have been drift corrected and the International Geomagnetic Reference Field removed. Short-wavelength, large amplitude anomalies in the eastern part of the map correspond to shallow (< 3 m) reversely magnetized Pliocene basaltic lavas. The down-thrown basalt west of the fault results in slightly longer wavelength anomalies west of the fault. Contour lines of elevation (meters) are provided and the two trenches across the SCFF are outlined. Three E-W profile lines (see Figure 6a-c) are shown. Map coordinates are in a Universal Transverse

Mercator (UTM), North American Datum 1983 (NAD83) projection.

Figure 4. Electrical conductivity map across the South Crater Flat fault (same area as Figures 2 & 3). Higher conductivities in the eastern part of the map correspond to shallow Pliocene basalt in the footwall of the SCFF. Anomalously low conductivities occur adjacent to the SCFF in a 140-200 m band (blue). Contour lines of elevation (meters) are provided and the two trenches across the SCFF are outlined. Map coordinates are in a UTM (NAD 83) projection.

Figure 5. Paleomagnetic results from sampled Pliocene basalts. Representative sample vector end-point demagnetization diagrams (Zijderveld, 1967) showing alternating field (a) and thermal demagnetization (b) of Pliocene basalt samples. Open and closed symbols are projections onto the vertical and horizontal planes, respectively. Gray boxes delineate the characteristic magnetization. Equal-angle projection (c) showing site mean directions and associated 95% cones of confidence for Pliocene basalts. Open symbols are projections onto upper hemispheres. Normal-polarity directions were inverted through the origin to their reverse-polarity counterparts.

Figure 6. Ground magnetic data (+), calculated anomaly based on forward modeling (heavy lines), and electrical conductivity data (light lines) are shown for E-W profiles at 4068700 N (a), 4068600 N (b), and 4068500 N (c) (see Figure 3 for profile locations). SCFF fault trace projected from depth is indicated on each profile (labeled vertical arrow). Unlabeled vertical arrows show projection of antithetic faults inferred from magnetic models. Note the correlation of lowest conductivity values with the fault zone.

Figure 7. E-trending EM-34 traverse, at approximately 4068700 N (line (a), figure 3), showing clear change in conductivity across the fault zone using 20 m-spaced coils, and horizontal (solid circles) and vertical dipoles (open circles). The horizontal dipole measurements are consistent with EM31 surveys along the same line (figure 6a). Vertical dipole measurements with 20-m-spaced coils yield higher conductivities and also indicate the location of the fault.

Figure 8. Expected soil conductivity as a function of the fraction of pore volume containing water (0.1 - 0.3), and pore water resistivity ($1 < \rho < 3$ (Ωm)), for alluvium with 40% porosity. The cause of the observed anomaly is indeterminate, but is most likely controlled by lateral variations in allostratigraphy. The Crater Flat alluvium (gray) has a lower observed bulk soil conductivity than the Late Black Cone alluvium (diagonal lines).

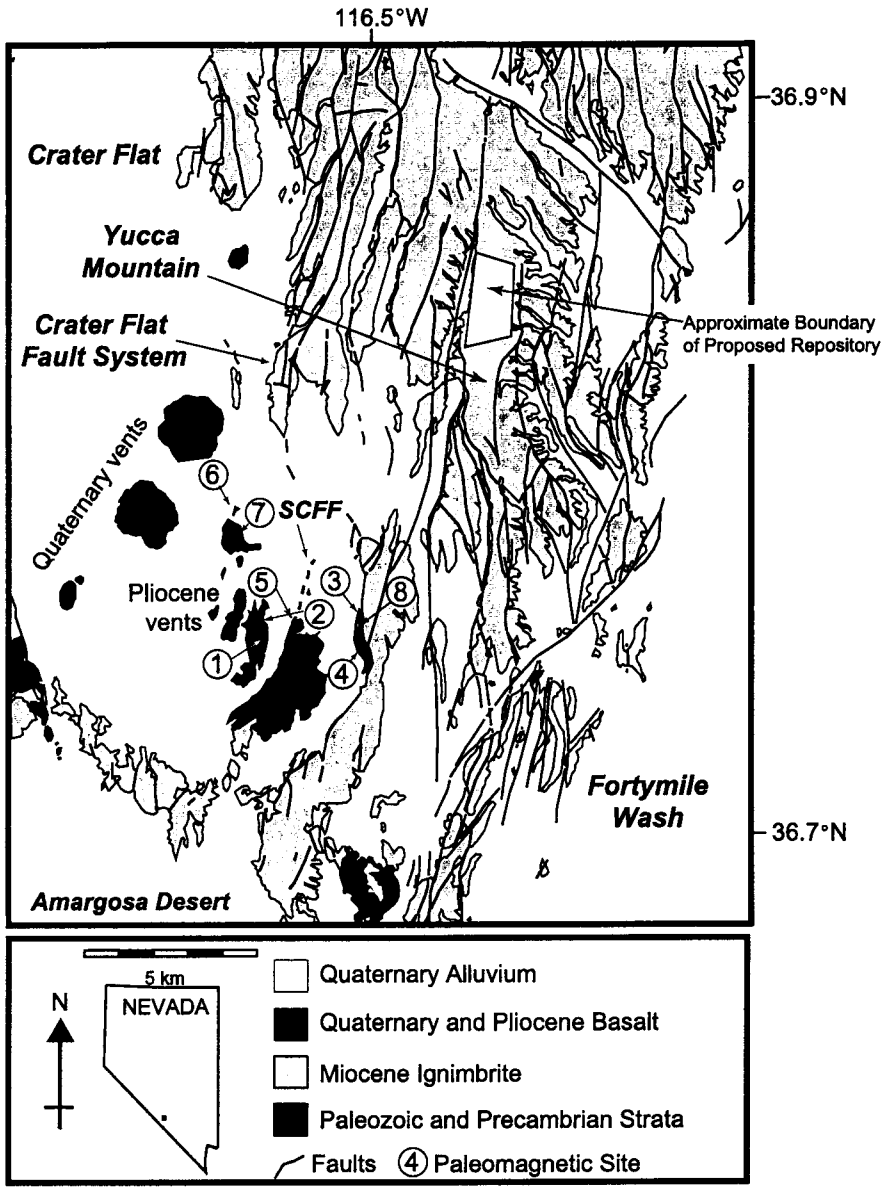

Figure 1
La Femina et al.

Table 1. Paleomagnetic Results From Pliocene Basalts, Crater Flat, Nevada

				In-Situ			
Site	n/N	R	M	Dec	Inc	k	α_{95}
PCF1	4/4	4	13.32	162.3	-63.0	47.4	13.5
PCF2	4/4	4	4.89	159.9	-68.5	41.9	14.4
PCF3	5/5	5	2.39	174.2	-61.7	79.3	8.6
PCF4	3/3	3	13.74	146.5	-62.7	39.6	19.9
PCF5	5/5	3	24.59	(266.0)	(-60.0)	(38.4)	(12.5)
PCF6	6/8	4	10.54	157.6	-46.8	56.5	9.0
PCF7	5/9	5	5.73	173.1	-65.5	156.8	6.1
PCF8	2/8	2	5.35	(184.3)	(-56.4)	(-.-)	(-.-)
Mean	**6/8**	**4**	**10.01**	**162.0**	**-61.7**	**81.9**	**7.4**

Notes: n is the number of samples that produced ChRM directions and N is the number of samples from the site demagnetized. R is the number of samples with reversed ChRM directions. M is the average NRM intensity in A/m. Dec and Inc are the declination and inclination of the site mean direction, in degrees. k is the Fisher (1953) precision parameter and α_{95} is the 95% confidence region about the mean value. Values in parentheses (PCF5 and PCF8) were not used in overall mean calculations because of suspected vertical axis rotation of the site or small number of ChRM directions for the site. Bold values indicate best estimate of mean direction for the Pliocene Basalts. Sample locations are shown on Figure 1.

Table 1
La Femina et al.

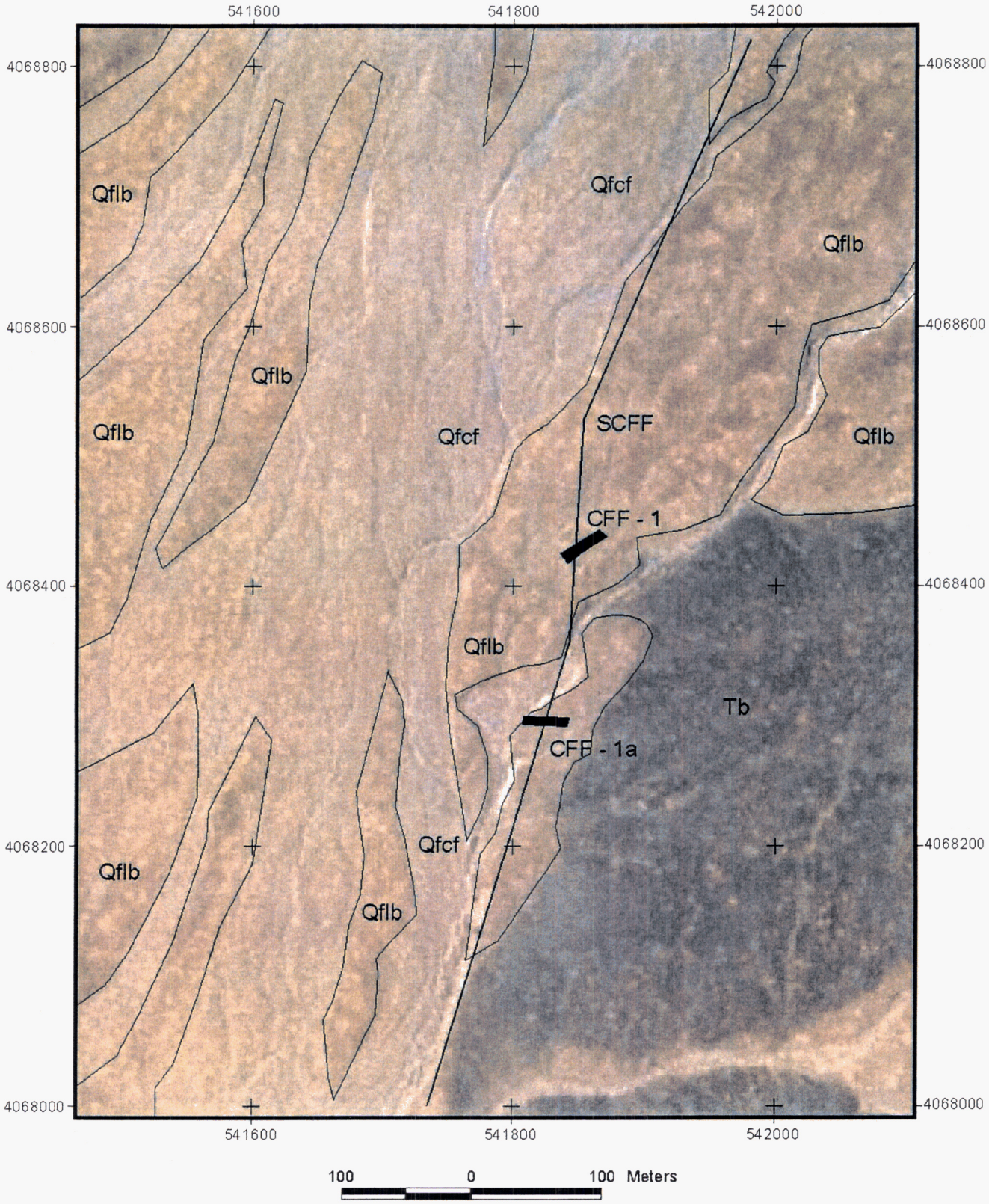

Figure 2
La Femina et al.

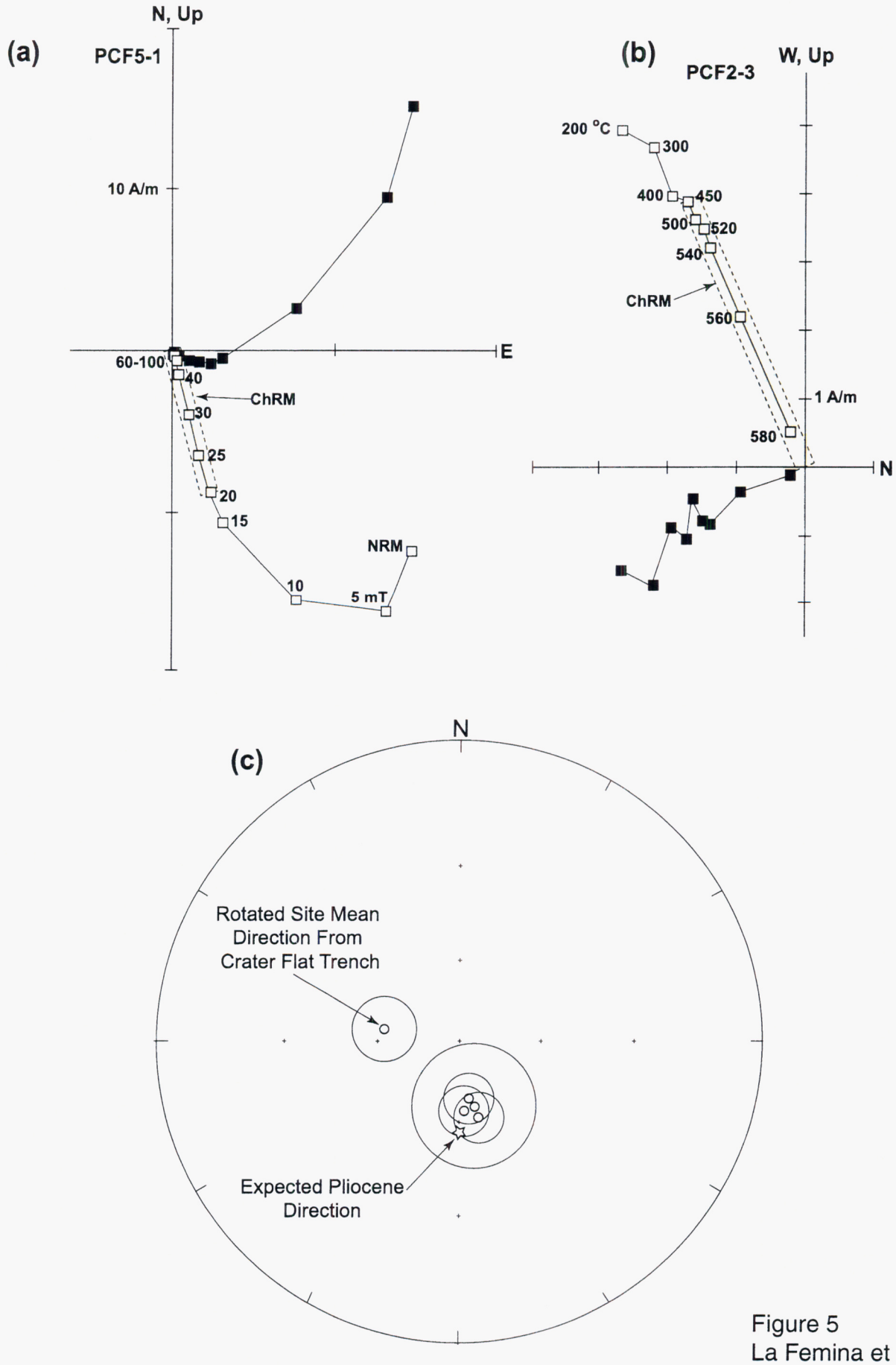

Figure 5
La Femina et al.

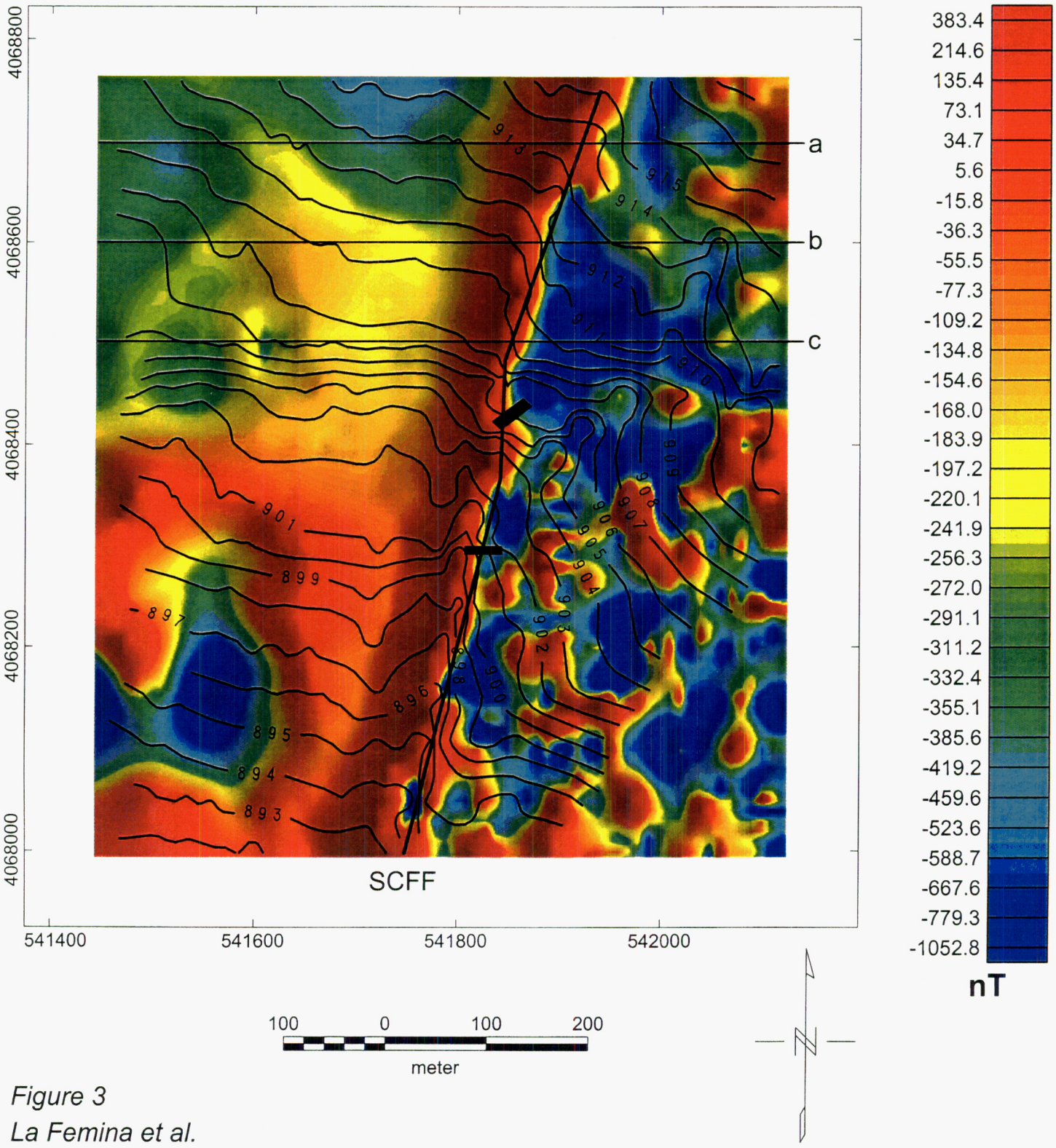

Figure 3
La Femina et al.

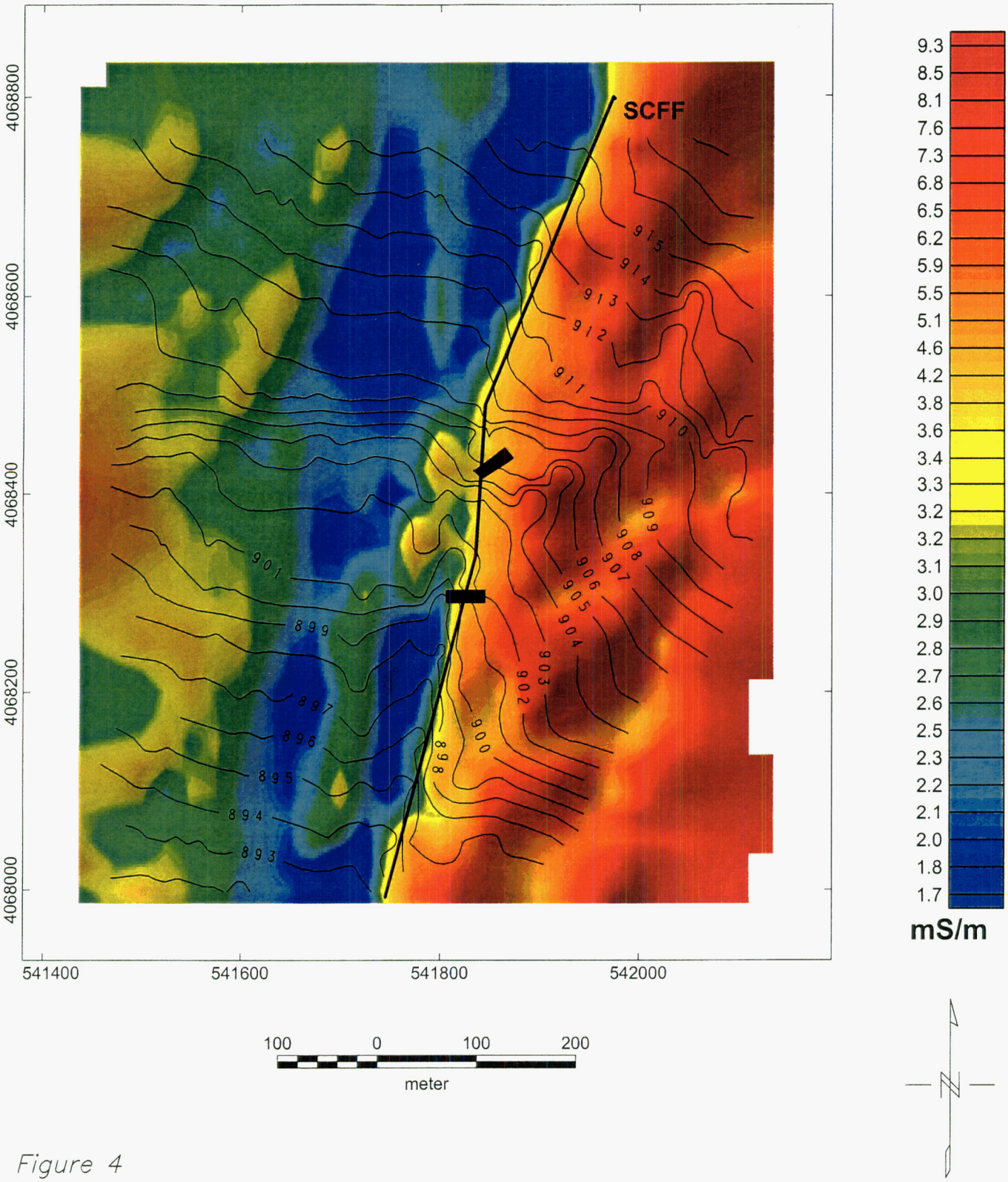

Figure 4
La Femina et al.

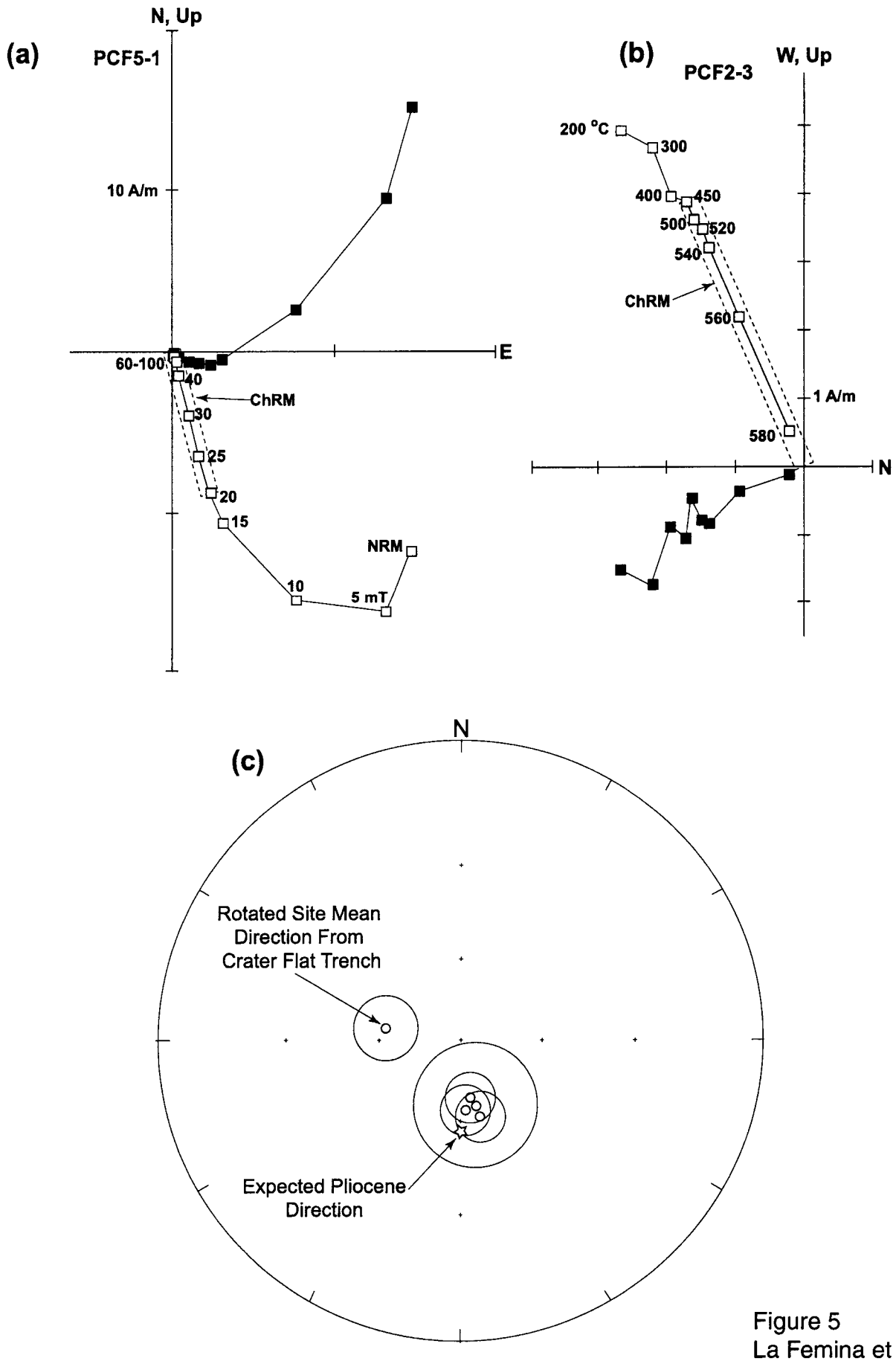

Figure 5
La Femina et al.

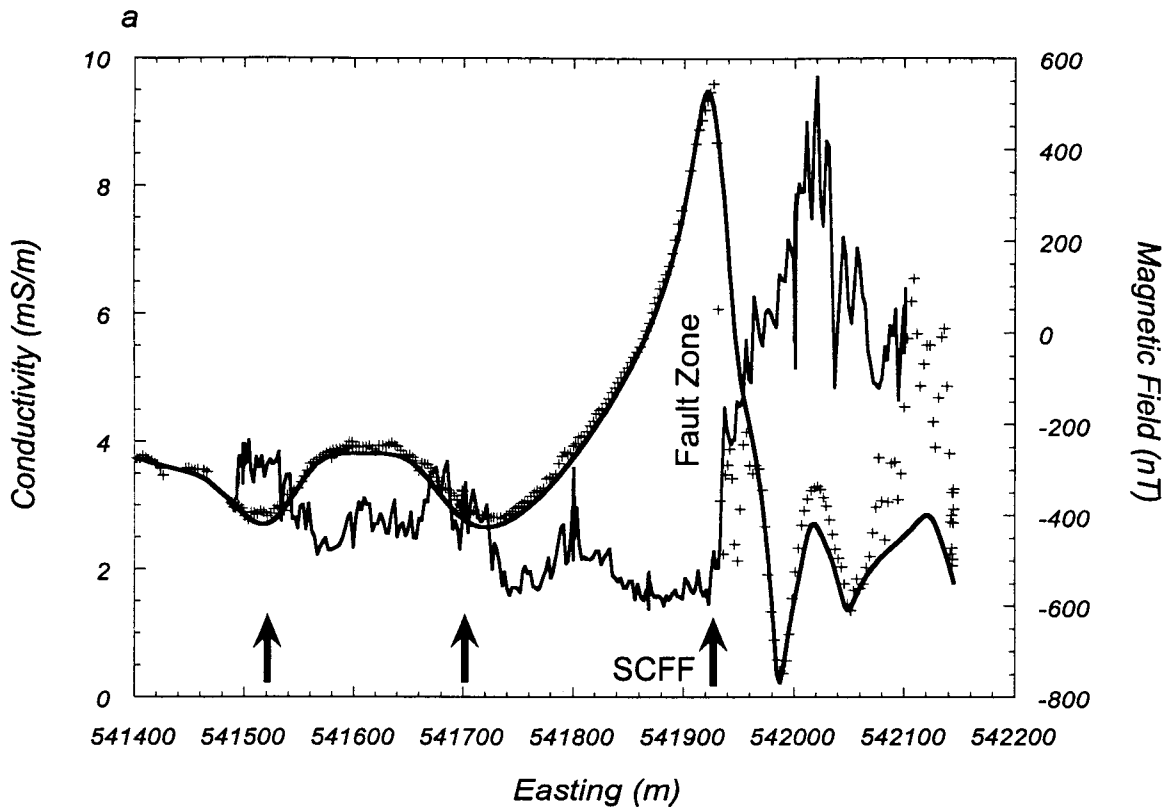

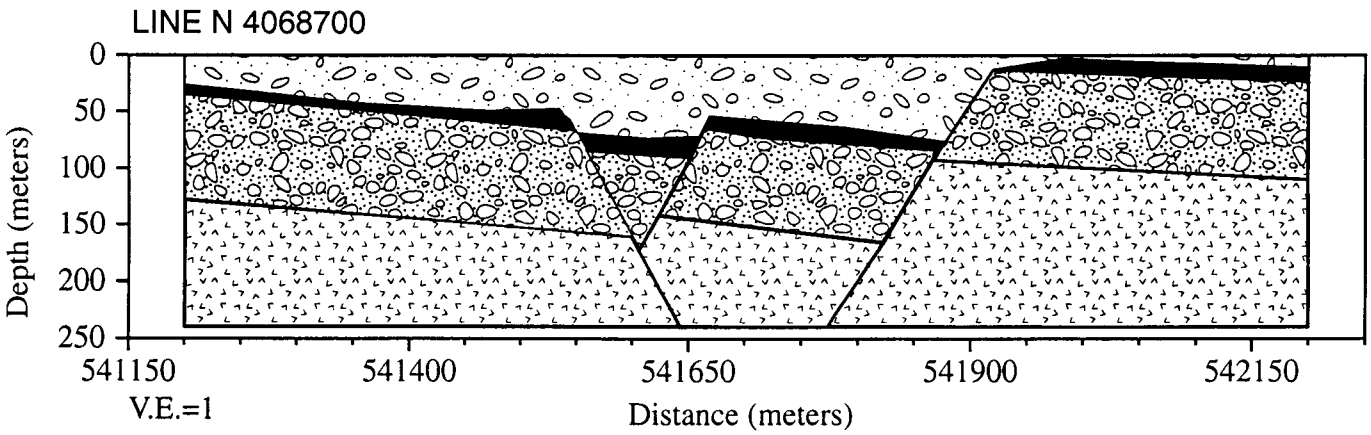

Late Tertiary/Quaternary Alluvium

Miocene-Pliocene Alluvium

Pliocene Basalt
MI = -62
MD = 162
NRM = 14 A/m

Tiva Canyon Tuff
MI = -55
MD = 170
NRM = 9 A/m

Figure 6a
La Femina et al.

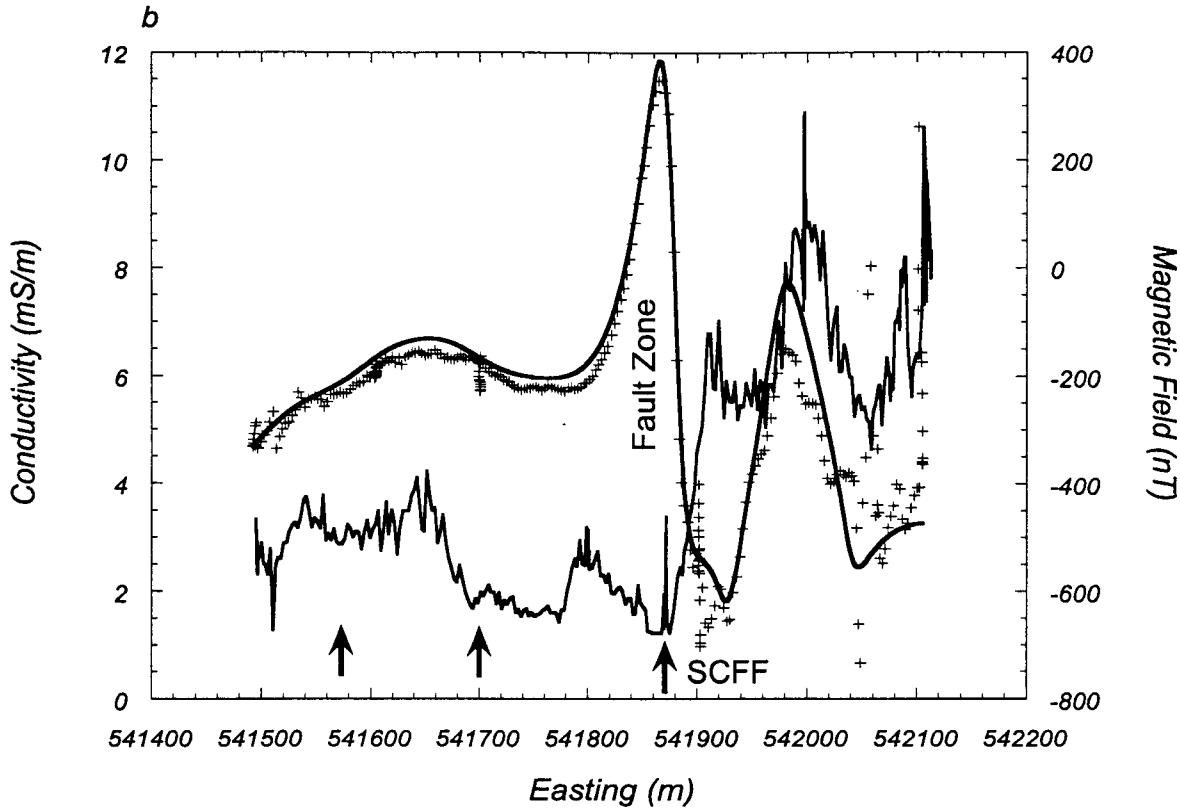

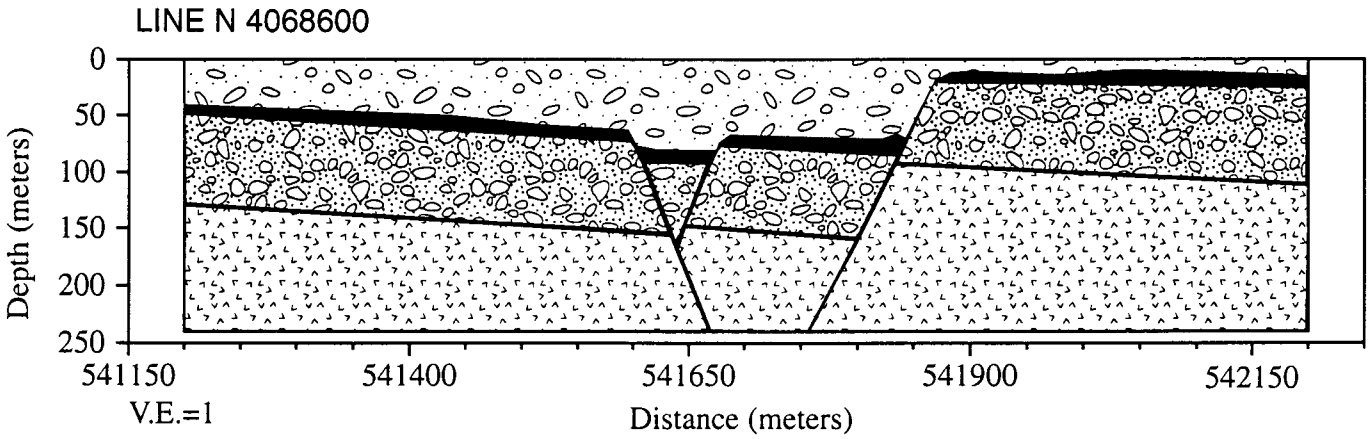

Late Tertiary/Quaternary Alluvium

Miocene-Pliocene Alluvium

Pliocene Basalt
MI = -62
MD = 162
NRM = 14 A/m

Tiva Canyon Tuff
MI = -55
MD = 170
NRM = 9 A/m

Figure 6b
La Femina et al.

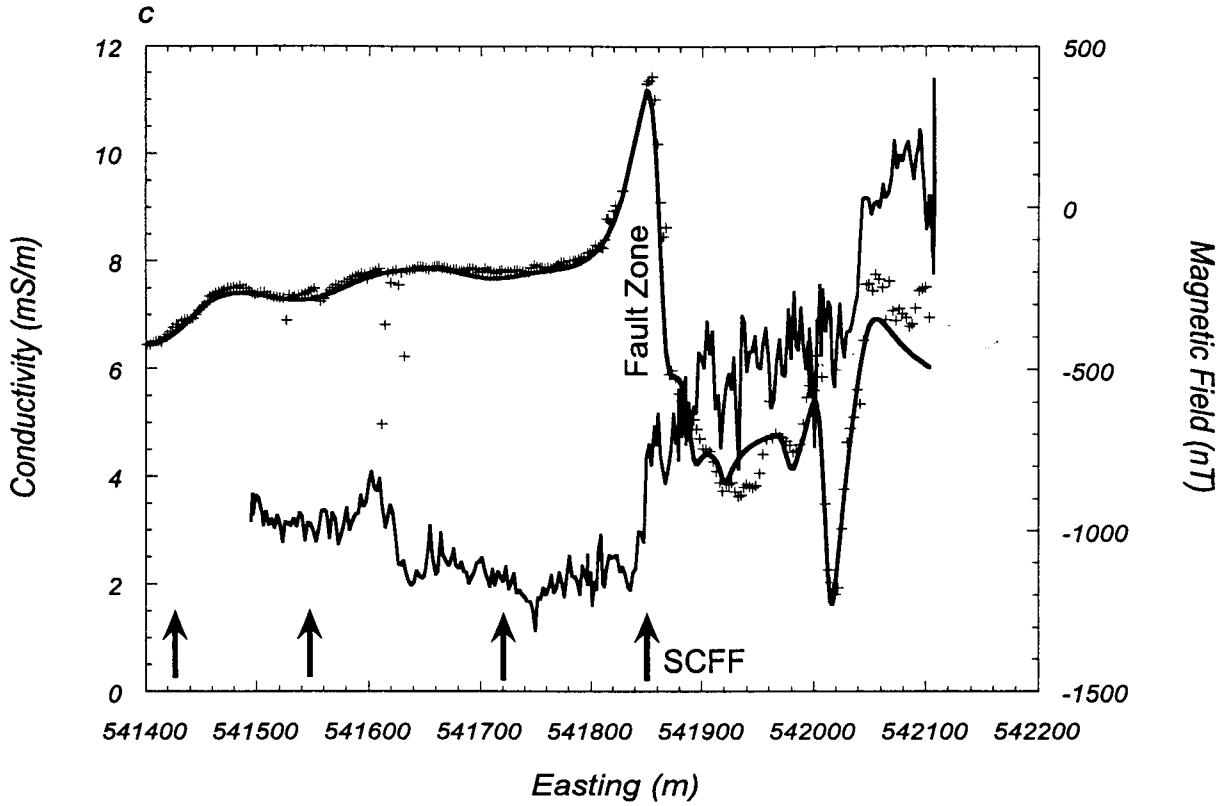

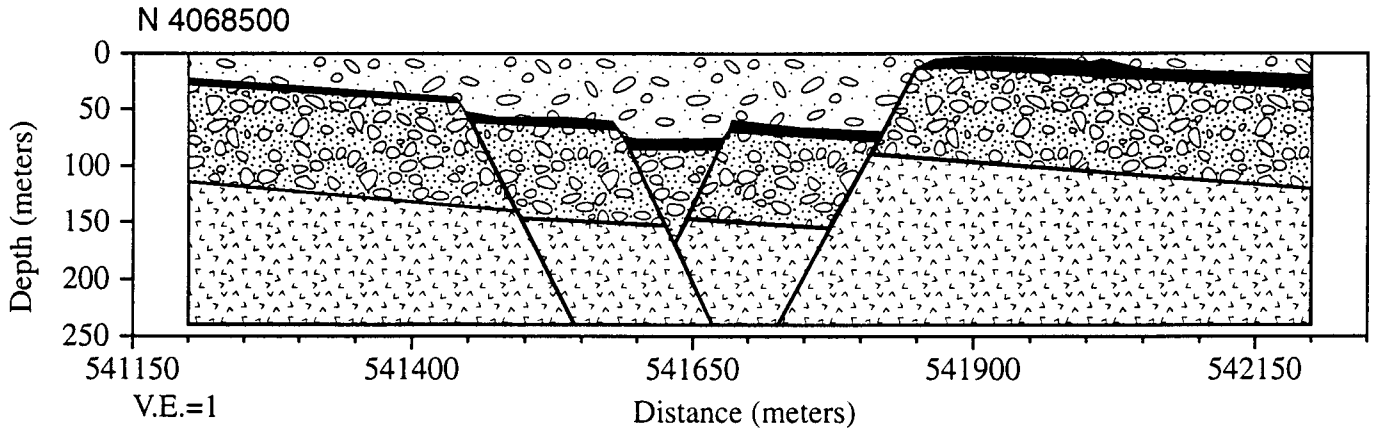

Late Tertiary/Quaternary Alluvium

Miocene-Pliocene Alluvium

Pliocene Basalt
MI = -62
MD = 162
NRM = 14 A/m

Tiva Canyon Tuff
MI = -55
MD = 170
NRM = 9 A/m

Figure 6c
La Femina et al.

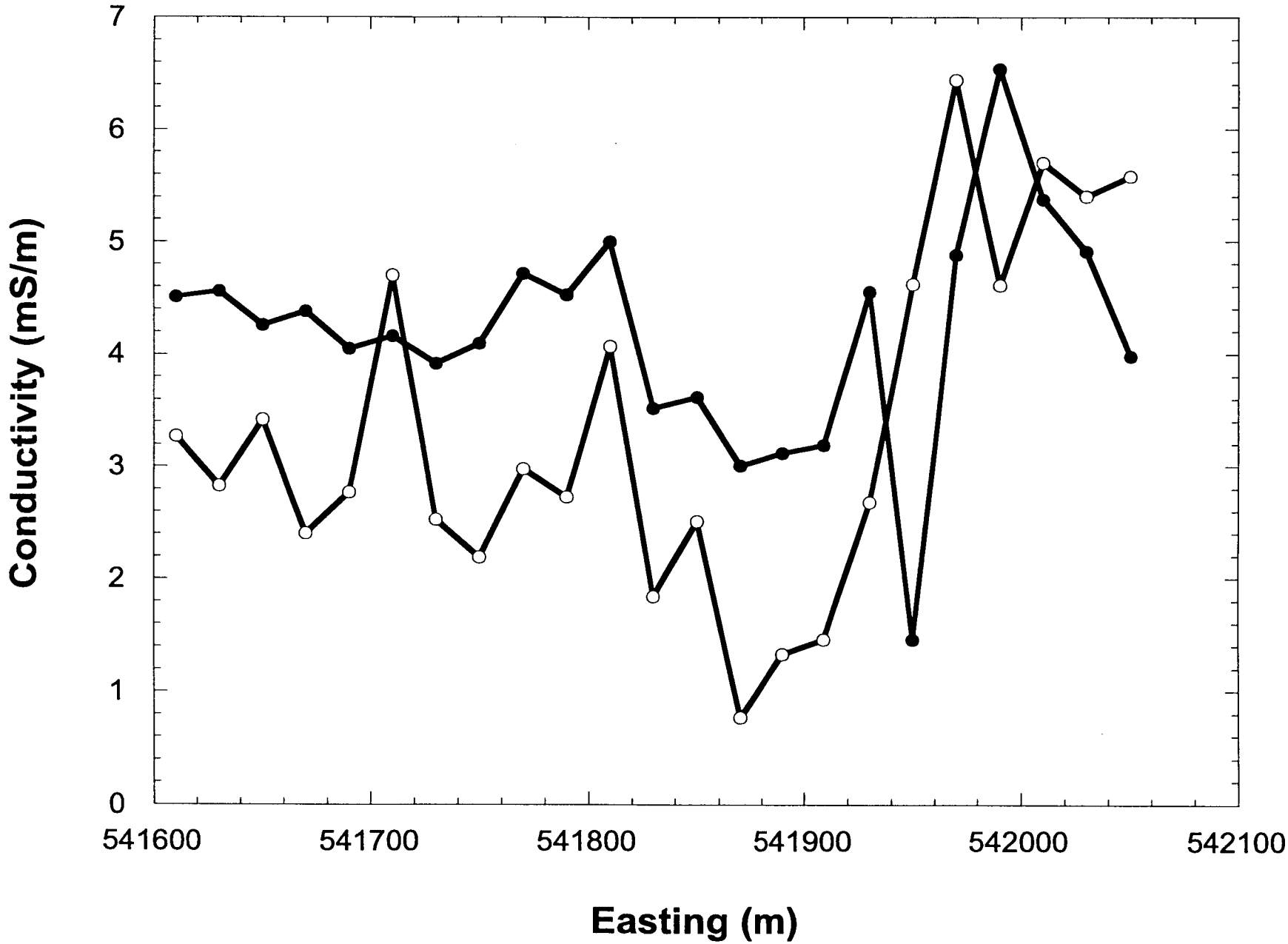

Figure 7
La Femina et al.

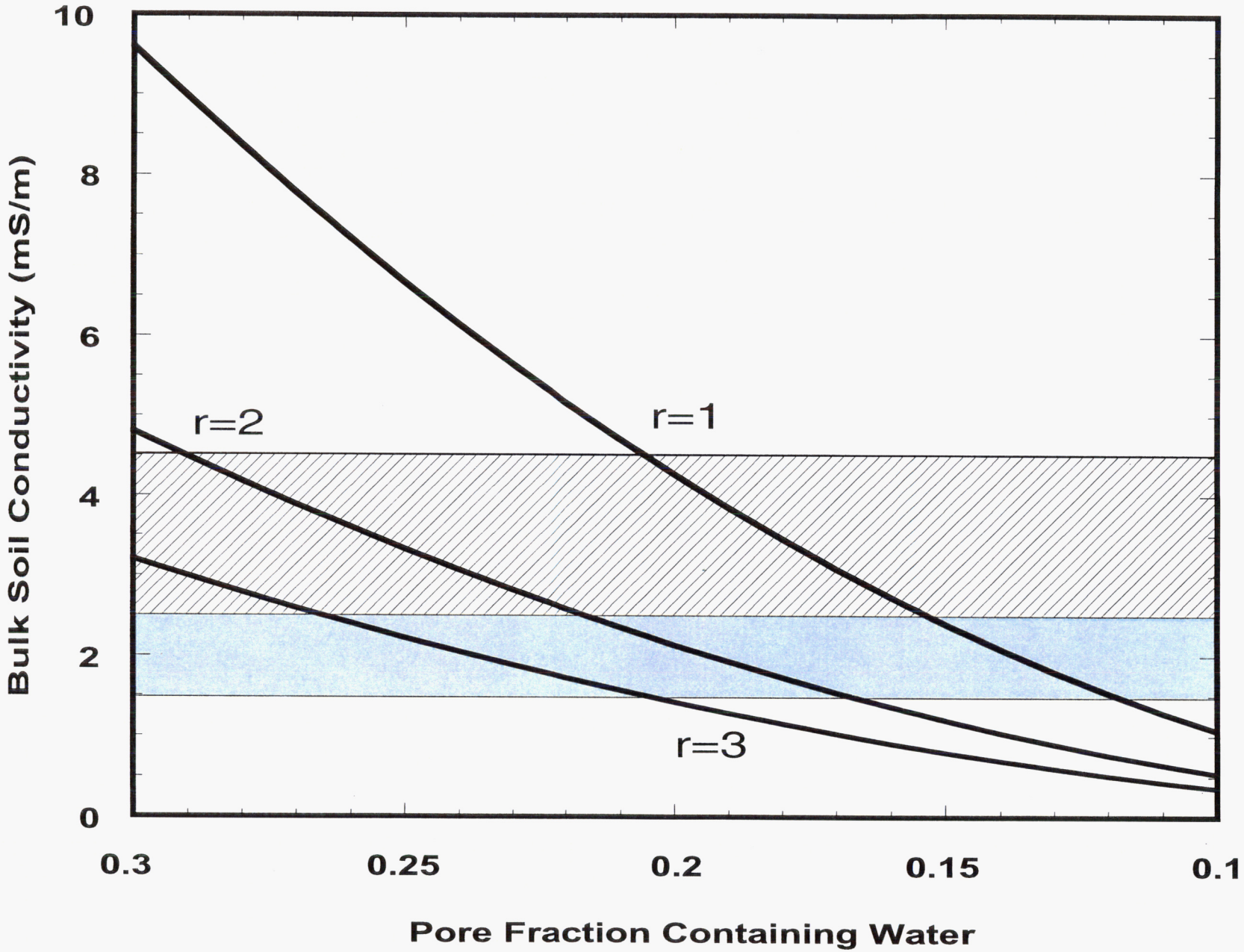

Figure 8
La Femina et al.

34/36